## University of Bristol - Explore Bristol Research
### General rights

# High Interfacial Hole-Transfer Efficiency at GaFeO$_3$ Thin Film Photoanodes

*Xin Sun, Devendra Tiwari,\* and David J. Fermin\**

The photoelectrochemical properties of polycrystalline GaFeO$_3$ (GFO) thin films are investigated for the first time. Thin films prepared by sol–gel methods exhibit phase-pure orthorhombic GFO with the *Pc*21*n* space group, as confirmed by X-ray diffraction and Raman spectroscopy. Optical responses are characterized by a 2.72 eV interband transition and sub-bandgap d–d transitions associated with octahedral and tetrahedral coordination of Fe$^{3+}$ sites. DFT-HSE06 electronic structure calculations show GFO is highly ionic with very low dispersion in the valence band maximum (VBM) and conduction band minimum (CBM). Electrochemical impedance spectroscopy reveals n-type conductivity with a flat band potential ($U_{fb}$) of 0.52 V versus reversible hydrogen electrode, indicating that GFO has the most positive CBM reported of any ferrite. The photoelectrochemical oxidation of SO$_3^{2-}$ shows an ideal semiconductor–electrolyte interfacial behavior with no evidence of surface recombination down to the $U_{fb}$. Surprisingly, the onset potential for the oxygen evolution reaction also coincides with the $U_{fb}$, showing interfacial hole-transfer efficiency above 50%. The photoelectrochemical properties are limited by bulk recombination due to the short-diffusion length of minority carriers as well as slow transport of majority carriers. Strategies towards developing high-efficiency GFO photoanodes are briefly discussed.

## 1. Introduction

Hydrogen generation through photoelectrochemical (PEC) water splitting is one of the most important and challenging concepts in electrochemical energy conversion. Over the last 5 years, important milestones have been achieved in terms of solar-to-hydrogen conversion efficiency for unassisted PEC systems based on integrated tandem III–V absorbers,[1–3]

reaching values as high as 19% under AM1.5 and 15% under concentrated solar illumination with power output as high as 27 W.[4,5] These systems demonstrate not only the feasibility of this concept but also the potential for scalability combining the electronic structure of the absorber with catalysts and protecting layers.[6,7] These advances also illustrate the challenges associated with designing new materials with appropriate optoelectronic properties, high chemical, and thermal stability, as well as amenable to scalable deposition methods.

Transition metal oxides have been widely considered as candidates for dimensionally stable photoelectrodes. Ferrite materials with bandgaps in the range of 2–2.7 eV are particularly attractive due to their chemical stability and Earth abundance.[8] Fe$_2$O$_3$ has been the most studied ferrite, showing a wide range of performances depending on deposition methods.[9] Other ferrite photoanodes include ZnFe$_2$O$_4$, MgFe$_2$O$_4$, and CuFe$_2$O$_4$, achieving external quantum efficiency values of close to 10% and photocurrent onset potentials ranging from 0.6 up to 1 V.[10,11] Ferrite photocathodes such as LaFeO$_3$ and YFeO$_3$ have shown very interesting photovoltages for the hydrogen evolution reaction, but their activity is limited by bulk and surface recombination losses.[12–17] Ferroelectric materials such as BiFeO$_3$ and Bi$_2$FeCrO$_6$ show complex PEC properties that have been linked to ferroelectric domains.[18,19] For instance, BiFeO$_3$ exhibits both n- and p-type conductivity, including above photovoltages larger than the bandgap.[20–22]

This article describes, for the first time, the unique PEC properties of GaFeO$_3$ (GFO), a ferrite widely investigated in the context of ferroelectric systems.[23–26] One of the unique aspects of this material is the high density of cation disorder due to the similar ionic radii of Ga$^{3+}$ and Fe$^{3+}$. Polycrystalline GFO thin films are prepared by sol–gel methods exhibiting a high degree of phase purity (orthorhombic with the *Pc*21*n* space group) featuring over 150 X-ray diffraction (XRD) peaks, as well as 25 different Raman modes that are assigned to Ga and Fe sites in octahedral and tetrahedral coordination. Indeed, a variety of sub-bandgap optical transitions observed in as-grown films are also consistent with both coordination geometries of Fe sites, suggesting a degree of elemental disorder. On the other hand, energy-dispersive X-ray spectroscopy (EDX) and X-ray photoelectron spectroscopy (XPS) analyses show identical Ga:Fe bulk and surface ratio, which is rather unusual in multicomponent transition metal oxides with the general formula ABO$_3$.

X. Sun, Prof. D. J. Fermin
School of Chemistry
University of Bristol
Cantocks Close, Bristol BS8 1TS, UK
E-mail: david.fermin@bristol.ac.uk

Dr. D. Tiwari
Department of Mathematics
Physics and Electrical Engineering
Northumbria University
Ellison Place, Newcastle upon Tyne NE1 8ST, UK
E-mail: devendra.tiwari@northumbria.ac.uk

The ORCID identification number(s) for the author(s) of this article can be found under https://doi.org/10.1002/aenm.202002784.

**ADVANCED
SCIENCE NEWS**
www.advancedsciencenews.com

**ADVANCED
ENERGY
MATERIALS**
www.advenergymat.de

The valence band spectrum is dominated by O 2p orbitals, as confirmed by DFT-HSE06 electronic structure calculations, demonstrating the strong ionic character of this ferrite. Differential capacitance data extracted from electrochemical impedance spectroscopy reveal an n-type conductivity with a flat band potential ($U_{fb}$) of 0.52 V versus the reversible hydrogen electrode (RHE), which is the most positive value reported for any ferrite. In the presence of $SO_3^{2-}$, GFO exhibits ideal semiconductor/electrolyte behavior, with no surface recombination, but limited by minority and majority carrier transport. Interestingly, the photocurrent onset potential for the oxygen evolution reaction (OER) coincides with $U_{fb}$, showing the highest interfacial charge transfer efficiency for polycrystalline thin films without the need for any cocatalysts. We also demonstrate that charge transport properties are highly sensitive to the Ga:Fe ratio, which opens new avenues for developing high-performance photoanodes.
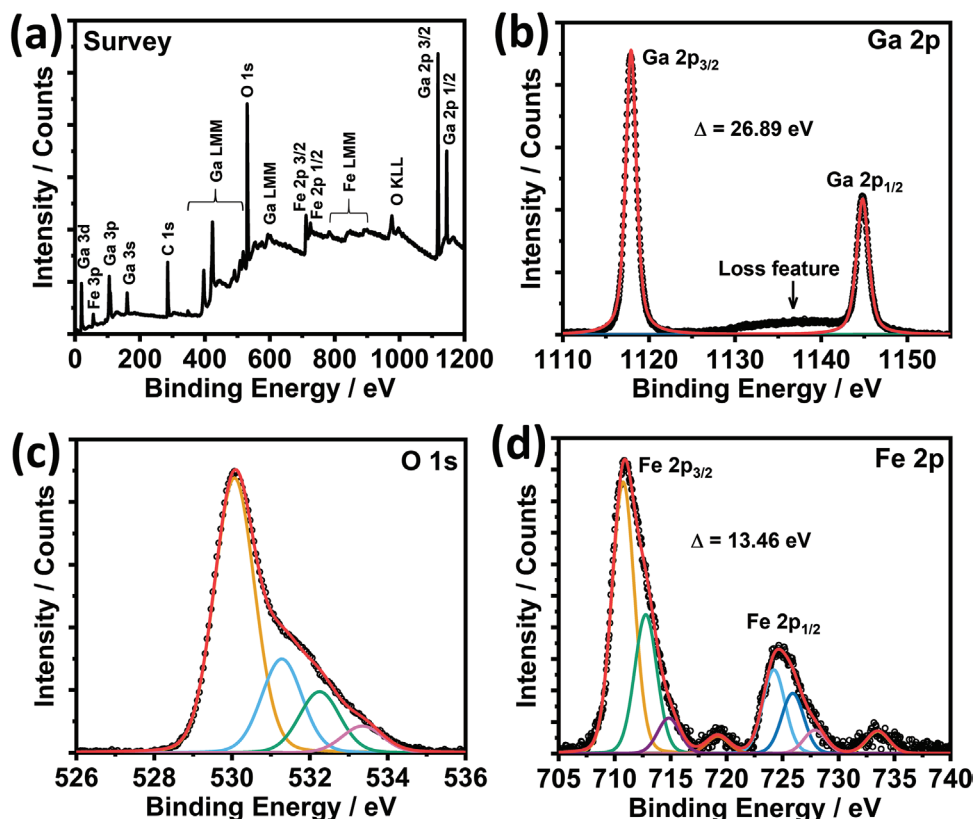
## 2. Results and Discussion

The complex structural properties of GFO prepared by thermolysis of a sol–gel precursor containing nitrate salts of both cations, citric acid, and ethylene glycol at 400 °C, followed by annealing at 600 °C in the air for 8 h (see Experimental Section),

are illustrated in **Figure 1**. The powder XRD pattern (Figure 1a) features over 150 Bragg reflections that closely match the standard pattern of orthorhombic GFO structure. The figure also shows the large number of reflections associated with the binary phases, $\varepsilon$-$Ga_2O_3$ and $\varepsilon$-$Fe_2O_3$, over the range of $2\theta$ values investigated. These results emphasize the need for high-quality XRD diffractograms and quantitative refinement to unambiguously demonstrate phase purity in this complex material. Figure 1a illustrates the full-profile Rietveld refinement of the experimental diffractogram to the orthorhombic GFO structure ($Pc21n$ space group), with correlation parameters $R_p$ = 5.11 and $R_{wp}$ = 3.06 and a rather flat difference curve. The estimated orthorhombic unit cell parameters are $a$ = 8.73589(72) Å, $b$ = 9.38098(74) Å, and $c$ = 5.07718(42) Å, with the unit cell consisting of 40 atoms equivalent to eight GFO formula units. The unit cell in Figure 1b exhibits four different crystallographic sites for metals atoms, including two with tetrahedral coordination and two with octahedral coordination. The octahedra form a network in the structure through shared terminals. The structural parameters obtained from the refinement are summarized in the crystallographic information file (CIF), which can be accessed from the crystallographic database through the CSD repository number 2025904. The analysis is consistent with previous neutron diffraction studies reported by Mishra et al.[27]
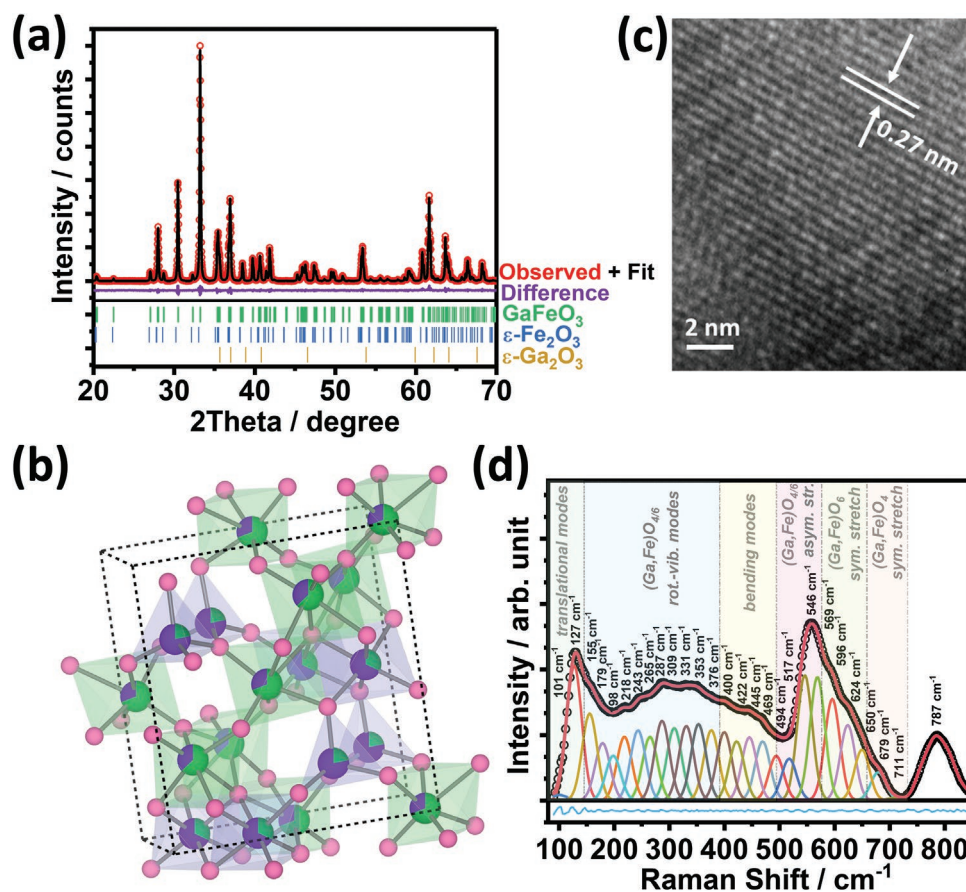


**Figure 1.** GFO structural complexity: a) powder XRD with quantitative Rietveld refinement to orthorhombic GFO ($Pc21n$ space group); b) schematic of the GFO unit cell, featuring Ga (purple) and Fe (green) sites with tetrahedral and octahedral coordination geometries; c) high-resolution transmission electron micrograph of GFO powder with lattice fringes associated with {221} planes; d) Raman spectrum of GFO films under 514 nm excitation, featuring 27 modes deconvoluted using Voigt functions.

**2002784** (2 of 9)

**ADVANCED
SCIENCE NEWS**
www.advancedsciencenews.com

**ADVANCED
ENERGY
MATERIALS**
www.advenergymat.de

**Figure 2.** Surface composition analysis of GFO thin films using XPS: a) survey spectrum showing the different photoemissions features; b) Ga 2p core-level; c) O 1s core-level; d) Fe 2p core-level. Spectral deconvolution is performed using Gaussian–Lorentzian mix functions.

One notable feature that is commonly observed in the GFO crystal structure is the mixed occupancy at the metal sites, which varies significantly with synthesis methods and condition. This arises because of the similar ionic radius of $Ga^{3+}$ and $Fe^{3+}$. This feature is a defining aspect of the PEC responses, as discussed further below. The crystalline nature of the GFO powders can be observed by the lattice fringes in the high-resolution transmission electron microscopy (HRTEM) image in Figure 1c, featuring a d-spacing of 0.27 nm, which is linked to {221} planes.

The Raman signature arising from the *C2v*(9) point group symmetry of orthorhombic GFO thin films is shown in Figure 1d. The spectrum was recorded for 350 nm thin film obtained by consecutive spin-coating, drying, and thermolysis steps, followed by annealing at the 600 °C in the air for 8 h (see Experimental Section). The spectrum is deconvoluted with ≈27 modes in the range of 100–800 cm, matching the modes reported in single crystals.[28] These are assigned to $Ga^{3+}$ and $Fe^{3+}$ in tetrahedral as well as octahedral coordinations with oxygen.[29–32] The stretching modes are observed between 500 and 750 cm with tetrahedral and symmetric stretches appearing at higher frequencies. The modes above 760 cm are likely due to $Ga^{3+}$.[33] The spectrum only shows a fraction of the 117 Raman active normal modes expected for a 40 atom unit cell, including 29 $A_1$, 30 $A_2$, 29 $B_1$, and 29 $B_2$.[28] However, this pattern is highly consistent with phase pure materials previously reported.[34,35]

The XPS survey spectrum in **Figure 2**a shows a variety of features, including prominent Ga (Ga $2p_{1/2}$, Ga $2p_{3/2}$, Ga 3s, Ga 3p, and Ga 3d), Fe (Fe $2p_{1/2}$, Fe $2p_{3/2}$, and Fe 3p), and oxygen

(O 1s) photoemission lines, as well as the corresponding Auger lines. Ga 2p (Figure 2b) shows the spin–orbit components of Ga $2p_{3/2}$ and $2p_{1/2}$ with a splitting of 26.9 eV, along with loss feature at around 1136 eV. Furthermore, the Ga $2p_{3/2}$ peak position at 1118 eV is characteristic of native gallium oxide, confirming that Ga is in a +3 oxidation state.[36,37] The main feature of the O 1s spectrum (Figure 2c) is centered at 530.01 eV, which is assigned to lattice bound oxygen,[13] while the other contributions are linked to surface hydroxyl and carbonylated groups.[38] Fe 2p core-level (Figure 2d) is significantly more complex to rationalize due to contribution from various phenomena such as multiple-splitting, multiple oxidation states, and charge transfer effects. As a first approximation, the most intense component in $2p_{3/2}$ is at 710.8 eV, with a 13.5 eV splitting from the $2p_{1/2}$ component, which is consistent with a Fe+3 oxidation state.[13,17] Other higher binding energy components can be linked to higher oxidation states; however, this would require further analysis of other Fe core-levels.[39] Interestingly, the observed surface Ga:Fe ratio of 1.17 is very close to the bulk ratio obtained from EDX spectrum (1.19, see Figure S1, Supporting Information) and XRD refined site occupancy (1.15, Figure 1a). This behavior is rather unusual for transition metal oxides with the general $ABO_3$ formula (such as perovskites), which often exhibit different A:B ratio in the bulk and at the surface.[38,40]

The optical properties of GFO thin films in the visible range are summarized in **Figure 3**. The absorption coefficient ($\alpha$), extracted from transmittance and reflectance spectra of 350 nm
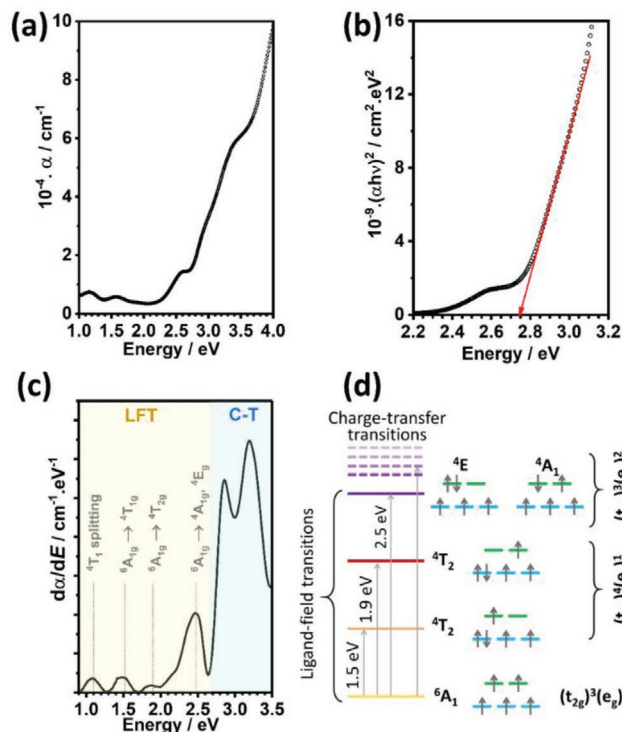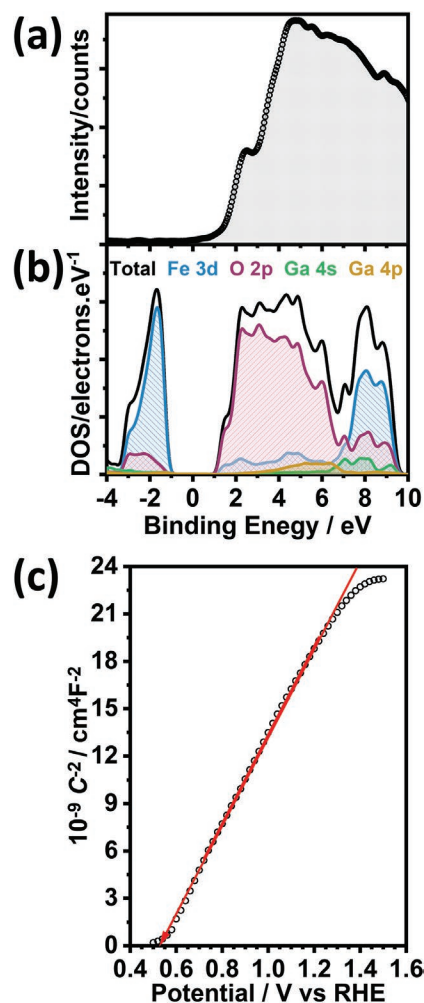
**Figure 3.** Optical properties of GFO thin films: a) absorption spectrum constructed from the transmittance and reflectance spectra (Figure S2, Supporting Information); b) Tauc plot for bandgap determination assuming direct band–band transitions; c) energy-differential absorption spectrum along with symmetry assignment for ligand-field (LFT) and charge-transfer transitions (C-T); d) modified TS diagram for $Fe^{3+}$ in tetrahedral and octahedral field depicting the electronic configuration of states associated with the optical transitions.



**Figure 4.** Bands composition and energy: a) valence-band spectrum of a GFO thin film measured under Al-K$\alpha$ X-ray excitation; b) DOS calculated using hybrid DFT (HSE06 functional). The Fermi level in the calculations is offset to coincide with the spectral response; c) Mott–Schottky plot constructed from electrochemical impedance spectroscopy data in Ar-saturated 0.1 M $Na_2SO_4$ aqueous solutions at pH 12.

films (Figure S2, Supporting Information) are displayed as a function of the photon energy, revealing several optical transitions between 1 and 3 eV (Figure 3a). The large $\alpha$ values indicate strong light capture cross section with energies larger than the optical band gap, which is characterized by a direct transition at 2.72 eV as estimated from the Tauc plot in Figure 3b. The energy differential plot of the absorption constant in Figure 3c reveals the various sub-bandgap features in the visible range, which correspond to ligand-field or charge-transfer transitions.[23] As described below, the valence band maximum (VBM) and conduction band minimum (CBM) of GFO are primarily made up of transition metal Fe-3d and O-2p states, where Fe coordinates in both tetrahedral and octahedral geometry; thus, the optical transitions can be described by merging Tanabe–Sugano (TS) diagrams of $Fe^{3+}$ in both coordination geometries (Figure 3d).[41] The prominent d–d forbidden transitions can be related to the presence of distortions in the lattice, which is a further manifestation in the cation disorder in the material.
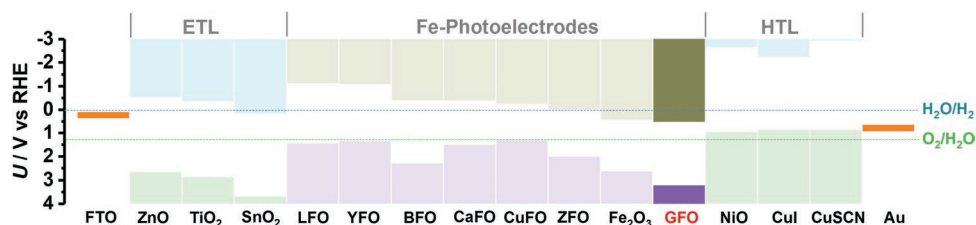
The valence band spectrum of GFO recorded using Al K$\alpha$ X-rays source as excitation is illustrated in **Figure 4**a. To rationalize these features, electronic structure calculations using density functional theory (DFT) with HSE06 functional were performed as described in the Experimental Section. The band diagram (Figure S3, Supporting Information) is characterized

by rather flat CBM and VBM, indicating high effective masses of charge carriers and, thus, low mobilities. The calculated bandgap of 2.65 eV agrees well with the experimental value. Figure 4b shows that the calculated density of states (DOS) and valence bandwidth reproduce the spectral response accurately, although the finer orbital features are not experimentally resolved due to the small cross section of the valence band states under X-ray excitation. The DFT calculations reflect the ionic nature of the oxide with the O 2p and Fe 3d states dominating the VBM and CBM, respectively. Only a small degree of hybridization is calculated in the valence (O 2p, Fe 3d, and Ga 4p orbitals) and conduction bands (Fe 3d and O 2p orbitals), thus indicating ionic nature of GFO.

A Mott–Schottky plot, constructed from the potential dependence of differential capacitance in Ar-saturated $Na_2SO_4$ aqueous solutions at pH 12 (Figure S4, Supporting Information), is displayed in Figure 4c. The positive slope reveals n-type semiconducting properties of as-grown GFO thin films, with a density

ADVANCED
SCIENCE NEWS
www.advancedsciencenews.com

ADVANCED
ENERGY
MATERIALS
www.advenergymat.de

**Figure 5.** Band alignment of GFO band edges with respect to common electron transport layer (ETL)[44] and hole transport layer (HTL).[44] Band offset with other Fe-based photoelectrodes including LaFeO$_3$ (LFO),[16] YFeO$_3$ (YFO),[17] BiFeO$_3$ (BFO),[45] CaFe$_2$O$_4$ (CaFO),[46] CuFeO$_2$ (CuFO),[47] ZnFe$_2$O$_4$ (ZFO),[48] and Fe$_2$O$_3$[49] illustrates how positive is the VBM in GFO.

of donor states ($N_D$) of $1.9 \times 10^{18}$ cm$^{-3}$. The linear Mott–Schottky plot over a range of 1 V and right down to the flat band potential strongly suggests a low density of sub-bandgap states near the CBM. The absence of Fermi level pinning is rather unusual in multicomponent semiconductor oxides,[42] in which cation and oxygen vacancies can generate a wide range of deep trap states.[43]
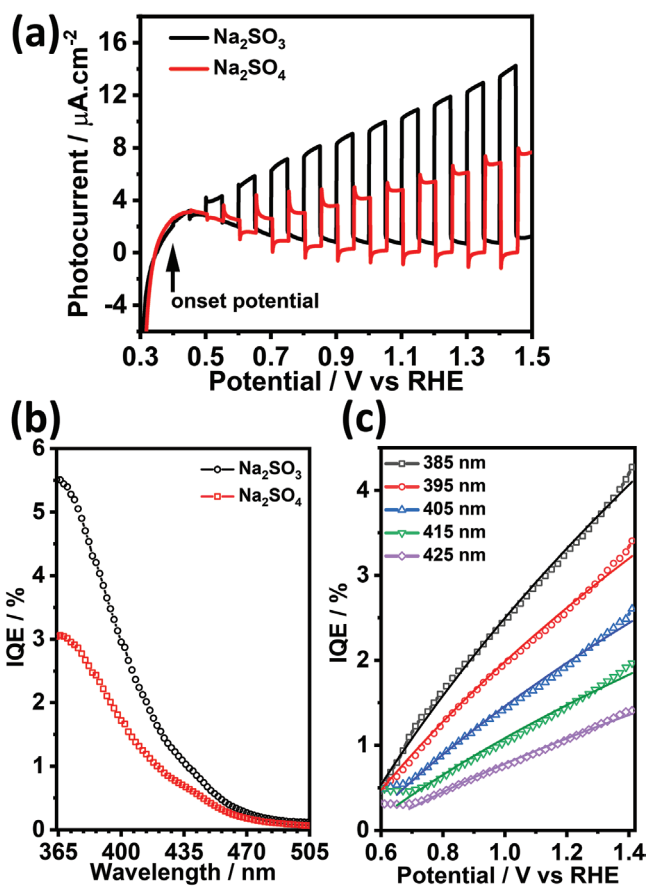
A $U_{fb}$ of 0.52 V versus RHE can be estimated from the Mott–Schottky plot, which, as illustrated in **Figure 5**, corresponds to a VBM value located at 3.22 V versus RHE. This is not only the most positive VBM reported for ferrite absorbers, but also even more positive than wide-bandgap oxides such as ZnO and TiO$_2$. This unusual band energetic can be rationalized in terms of the effect of the FeO$_6$ octahedral tilting on the energy of the O 2p orbitals.[50] The ionic radius of gallium (0.62 Å) is significantly smaller than other A-site elements, such as La (1.36 Å), Y (0.9 Å), and Bi (1.03 Å); thus, the Fe–O–Fe angle is less than 180° leading to the decrease of VBM. Furthermore, based on the model proposed by Meng et al.[51] rather electronegative A-site cations (such as Ga$^{3+}$) tend to lower the CBM in FeO$_6$ coordinated structures with a low degree of hybridization. Figure 5 also shows the band alignment of GFO with common electron-transporting layer (ETL) and hole-transporting layer (HTL), indicating that establishing semiconductor junctions with appropriate band alignment will require unconventional materials.

The unique structure and optical and electronic properties of GFO thin films bring about a very unusual PEC behavior as described in **Figure 6**. Figure 6a contrasts the current–voltage characteristics of a 350 nm GFO thin film under chopped illumination (405 nm) in Ar-purged 0.1 M Na$_2$SO$_3$ and 0.1 M Na$_2$SO$_4$ solutions (pH 12). The photocurrent onset-potential (photovoltage) is between 0.4 and 0.5 V versus RHE in both electrolytes, which is remarkably close to the $U_{fb}$. The magnitude of the photocurrent responses is larger in the presence of SO$_3$$^{2-}$, a strong hole scavenger that can effectively suppress surface recombination.[52] The photocurrent decay in the light on-transients and the negative overshoot in the off-transient in the SO$_4$$^{2-}$ solution are also evidence of surface recombination competing with the OER.[52] The photocurrent ratio between both electrolytes is a measure of the interfacial hole-transfer efficiency towards OER, the so-called surface charge transfer efficiency (SCTE).[53] In the case of 350 nm GFO films, the SCTE value is 55% at 1.23 V versus RHE, which is significantly larger than other ferrites photoanodes such as CaFe$_2$O$_4$ (5%) and ZnFe$_2$O$_4$ (10–40%).[10] The internal quantum efficiency (IQE) spectra recorded at 1.4 V versus RHE in Figure 6b, as well as the corresponding Tauc representation (Figure S5, Supporting

Information), are strongly consistent with the estimation of the optical band gap (2.7 eV), further confirming that sub-bandgap transitions do not generate free charge carriers.

The absence of surface recombination in the presence of SO$_3$$^{2-}$ allows rationalizing the photocurrent–voltage characteristics in terms of the Gaertner expression[52,54,55]

$$IQE = 1 - \frac{e^{(-\alpha W)}}{1 + \alpha L_n} \tag{1}$$



**Figure 6.** PEC responses of 350 nm GFO thin films: a) linear sweep voltammetry recorded at 5 mV s$^{-1}$ under square wave 405 nm light perturbation and $4.25 \times 10^{15}$ cm$^{-2}$ s$^{-1}$ photon flux in Ar-saturated 0.1 M Na$_2$SO$_3$ and Na$_2$SO$_4$ electrolytes (pH 12); b) IQE at 1.4 V versus RHE as a function of wavelength; c) potential dependence of IQE in Ar-saturated 0.1 M Na$_2$SO$_3$ electrolytes (pH 12), along with fits to the Gaertner model (Equation (1)), consistent with a hole-diffusion length $L_n = 12.5 \pm 0.3$ nm.

where $W$ is the width of the space charge region, and $L_n$ is the holes diffusion length. The fit to the IQE–voltage curves at different wavelengths in Figure 6c was obtained using Equation (1), the $\alpha$ values displayed in Figure 3a, while $W$ is calculated from the Schottky equation[54,55]

$$W = \sqrt{\left[\frac{2\varepsilon\varepsilon_0}{qN_D}(U_{fb} - E)\right]} \qquad (2)$$

employing the experimental values of $U_{fb}$ and $N_D$. From this analysis, a $L_n = 12.5 \pm 0.3$ nm can be estimated across the range of wavelengths. The fact that Equation (1) reproduces the experimental curves down to the $U_{fb}$ confirms that surface recombination is negligible in the presence of $SO_3^{2-}$. On the other hand, the very short $L_n$ indicates that photoelectrode efficiency is primarily limited by bulk recombination. This conclusion is consistent with the very low band dispersion (Figure S3, Supporting Information), which induces heavy effective masses of electrons and holes.

Further evidence of the role of carrier transport in the photocurrent responses can be elucidated from the thickness dependence and illumination direction shown in **Figure 7**. The photocurrent magnitude increases with an increasing thickness (Figure 7a), which is determined by the number of coating steps (see Experimental Section). The photocurrent magnitude increases by a factor of three upon increasing the film thickness

from 110 to 350 nm. Based on the optical constant (Figure 3a), the penetration depth of light at a wavelength of 405 nm ($1/\alpha$) is ≈500 nm. Thus, increasing film thickness in this range effectively increases the flux of carrier generation. Figure 7b shows that 350 nm films exhibit twice larger photocurrents under back illumination (through the FTO coated glass) than under front illumination (through GFO/electrolyte junction). On the other hand, the difference between front and back illumination is very small in 110 nm films (Figure 7c). Photocurrent transients in Figure S6, Supporting Information, also show a slower rise time and decay in the 350 nm films, while the 110 nm film displays a sharper response. These results clearly indicate that electron transport in these films is also a key limiting factor in the performance of these materials, which may arise not only from intrinsically low mobility but also the presence of deep trap states.[56]

Finally, Figure 7d illustrates the strong effect of the Ga:Fe ratio on the PEC responses. Decreasing Ga:Fe ratio from 1.5 to 0.54 leads to a tenfold increase in photocurrent, suggesting that the nature of trap states may be connected to Ga sites. The Ga:Fe ratios reported in Figure 7d correspond to the composition of the sol–gel precursor. Analysis of the film composition reveals small variations of ≈10% with respect to the Ga:Fe ratio in the sol–gel precursor. Representative XRD patterns (Figure S7, Supporting Information) show no clear evidence of the binary oxide phase in this range of compositions, although the Ga–Fe–O phase diagram is very rich as a result
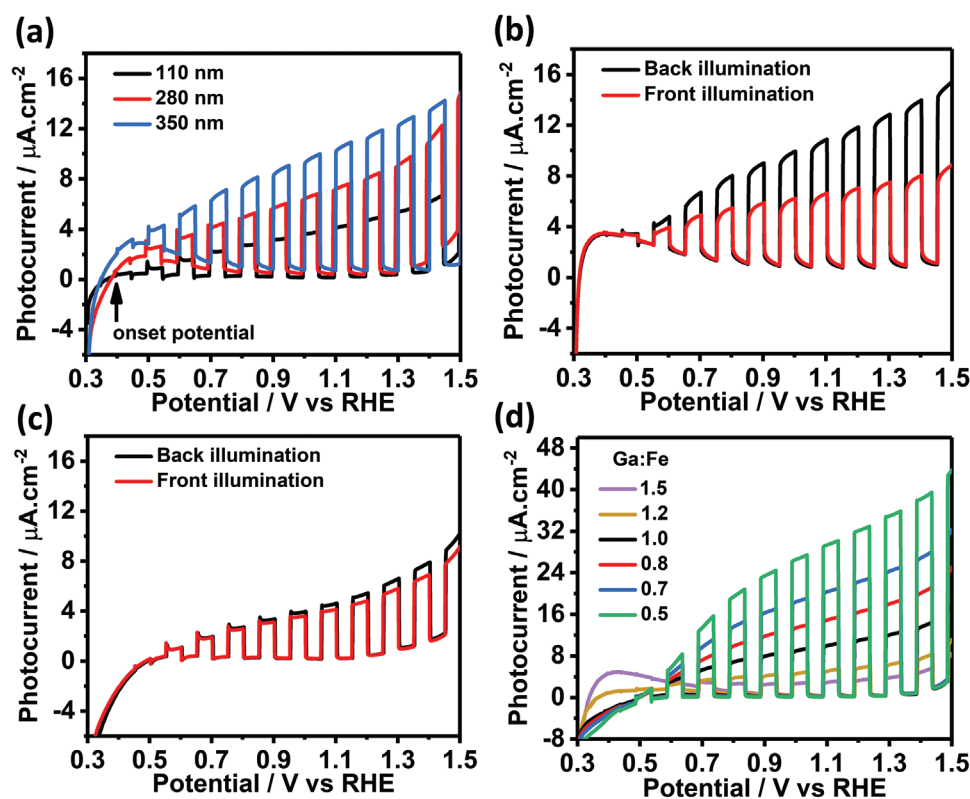


**Figure 7.** Thickness and composition dependence of photocurrent responses, measured in Ar-saturated 0.1 M $Na_2SO_3$ aqueous solutions at pH12: a) linear sweep voltammetry responses of films with a thickness between 110 and 350 nm; photocurrent responses under the back and front illumination at b) 350 nm and c) 110 nm films; d) photocurrent responses as a function of Ga:Fe ratio in the sol–gel precursor. Scan rate, wavelength, and photon flux values are as indicated in Figure 6a.

**ADVANCED
SCIENCE NEWS**

www.advancedsciencenews.com

**ADVANCED
ENERGY
MATERIALS**

www.advenergymat.de

of the similar ionic radii of both cations.[57,58] Cyclic voltammograms recorded as a function of the GFO composition (Figure S8, Supporting Information) show that decreasing the Ga/Fe ratio systematically shifts the flat-band potential towards more negative values, which is also consistent with the model proposed by Meng et al.[51] Beyond the limitations imposed by bulk recombination losses, the relatively large bandgap of GFO (2.7 eV) would limit the performance of this material to values in the range 5% solar-to-hydrogen efficiency according to the analysis by Fountaine et al.[59] However, the tunability of the band edges with the Ga:Fe ratio enables the implementation of new strategies towards high-efficiency photosystems including: 1) improving carrier collection and light capture cross section by depositing ultrathin GFO layers onto highly textured electron transporting layers; and 2) tuning band alignment in multijunction tandem devices.

## 3. Conclusions

Solution-processed GFO thin films exhibit unusual PEC properties, including high surface charge transfer ratio towards the OER, which manifests itself by a photocurrent onset potential close to the flat band potential (between 0.4 and 0.5 V vs RHE). We are not aware of any other semiconductor material capable of evolving oxygen at the flat-band potential in the absence of protecting layers and cocatalysts. In the presence of $SO_3^{2-}$ ions acting as hole scavengers, no evidence of surface recombination is observed. Based on the Gaertner model, a hole diffusion length of 12.5 ± 0.3 nm can be estimated under a range of wavelengths close to the bandgap. The ideal behavior of the GFO/electrolyte junction is also observed in capacitance–potential curves, which follows the Mott–Schottky equation for more than 1 V down to the flat-band potential. The CBM is located 0.52 V versus RHE, which is the most positive CBM reported for any ferrite. DFT-HSE06 calculations show that this material is highly ionic, and the relatively positive CBM can be rationalized in terms of Coulombic potential generated by the $Ga^{3+}$ cation. Our study also shows that the similar ionic radii of $Ga^{3+}$ and $Fe^{3+}$ ion introduces significant complexity in the material structure, featuring tetrahedral and octahedral coordination of the cations, which manifest themselves in multiple Raman modes and optical transitions. The GFO photoresponses are dominated by bulk recombination losses, linked to low carrier mobility resulting from low band dispersion and deep trap states. Our results also show that bulk recombination is significantly decreased in Ga-poor films. These experimental and computational results demonstrate not only the potential of this material as photoanodes but also the tunability of its electronic properties and the potential for integration into highly efficient PEC devices.

## 4. Experimental Section

*GFO Thin Film Preparation*: GFO thin films were synthesized following a modified sol–gel method.[13] First, 0.5 M $Ga(NO_3)_3 \cdot 6H_2O$ aqueous solution (1 mL) and 0.5 M $Fe(NO_3)_3 \cdot 9H_2O$ aqueous solution (1 mL) were mixed under strong stirring at 60 °C for 1 h. 1 M citric acid ethanolic

solution (1 mL) and ethylene glycol (62.5 mL) were subsequently added, and the solution was further stirred overnight in a capped glass vial. The precursor solution was spin-coated onto clean $F:SnO_2$ (FTO) conductive glass at 3000 rpm for 30 s, followed by drying at 100 °C for 10 min and thermolyzing the metal-complex at 400 °C for 1 h, to deposit 1 layer of GFO. Thicker films were obtained by repeating the same procedure and building the thickness layer-by-layer. The final films were annealed at 600 °C for 8 h to obtain crystalline GFO thin films. The $Ga^{3+}$ and $Fe^{3+}$ precursors were stoichiometrically changed following $Ga_{2-x}Fe_xO_3$ (x from 0.8 to 1.3) compositions to prepare the thin films with different Ga:Fe ratio.

*Characterization Methods*: Crystal structure was probed using powder XRD with Cu Kα radiation (λ = 1.54016 Å; Bruker AXS D8 ADVANCE). Scanning electron microscopy (SEM, JEOL IT300) revealed the morphology and film thickness. Energy-dispersive X-ray detector coupled to the SEM (Oxford X-Max-80 detector) was used to quantify Ga and Fe content. HRTEM was carried out in a JEOL JEM 2100. Reflectance and transmittance spectra in the UV–visible region were measured by a Shimadzu UV-2600 spectrophotometer. XPS of GFO thin-film was recorded at the Bristol NanoESCA Facility. The configuration included an ultra-high vacuum chamber pumped below a base-pressure of $4 \times 10^{-11}$ mbar, a non-monochromatic Al Kα X-rays source as excitation, and an ARGUS spectrometer with an overall energy resolution of 0.9 eV, for photoelectron detection. High-resolution scans of the core levels and survey scans were collected on "as-received" film with 20 and 50 eV pass energies, respectively. The films exhibit considerable charging, which was compensated using charge neutralization through electron flood gun. The charge correction on the measured spectra was applied, assuming the C 1s peak at 284.8 eV. The spectra were deconvoluted by Gaussian–Lorentzian mixture peaks after a Shirley background removal using XP SPEAK code.

Electrochemical impedance spectroscopy of GFO film in $Na_2SO_4$ aqueous electrolyte was performed with Modulab potentiostat and frequency response analyzer. The frequency scans were acquired with 13 mV (RMS) AC modulation between 1.7 Hz and 11.7 kHz. PEC experiments were carried out in Ar-purged aqueous solutions containing 0.1 M $Na_2SO_4$ or $Na_2SO_3$ at pH 12. The dark and photocurrent–voltage measurements were conducted with an Ivium CompactStat potentiostat, using three-electrode configuration (working electrode, carbon counter-electrode, and Ag/AgCl reference electrode). All potentials are referred to against the RHE. For photocurrent transients, the films were illuminated with a 405 nm light-emitting diode (Thorlabs) driven by a Stanford Research Systems waveform generator. The lock-in amplifier (Stanford Research Systems SRS 830)-based photocurrents with potential dependence and spectral response were acquired under a 27 Hz chopped illumination by a 100 W quartz halogen lamp (Bentham ILD-D2-QH) through a monochromator (Bentham TMc300). The photon flux from both the light sources was measured by a calibrated Si photodiode (Newport Corporation).

*Computational Methods*: GFO electronic structure calculations were carried out using the CASTEP and HSE06 functional-based hybrid-DFT methodology.[60,61] Norm-conserving pseudopotentials with an energy cutoff of 1100 eV and Monkhorst-Pack k-point grid spaced <0.02 Å were employed throughout the calculations. For structure optimization, strict convergence criteria were implemented, including energy and force tolerances of 1 neV and 1 meV Å$^{-1}$, respectively. The optimized unit cell has orthorhombic symmetry ($Pc21n$) and dimensions within 1% of experimental results. The band structure and DOS calculations were also performed with the same energy convergence and parameters.

## Supporting Information

Supporting Information is available from the Wiley Online Library or from the author. All data presented in this paper can be freely accessed from the Bristol's Research Data Repository, data.bris, at https://doi.org/10.5523/bris.c4w8vwn8xfr2kozw9k8lb7o1.

## Conflict of Interest

The authors declare no conflict of interest.

[1] J. L. Young, M. A. Steiner, H. Döscher, R. M. France, J. A. Turner, T. G. Deutsch, *Nat. Energy* **2017**, *2*, 17028.

[2] M. M. May, H. J. Lewerenz, D. Lackner, F. Dimroth, T. Hannappel, *Nat. Commun.* **2015**, *6*, 8286.

[3] E. Verlage, S. Hu, R. Liu, R. J. R. Jones, K. Sun, C. Xiang, N. S. Lewis, H. A. Atwater, *Energy Environ. Sci.* **2015**, *8*, 3166.

[4] W. H. Cheng, M. H. Richter, M. M. May, J. Ohlmann, D. Lackner, F. Dimroth, T. Hannappel, H. A. Atwater, H. J. Lewerenz, *ACS Energy Lett.* **2018**, *3*, 1795.

[5] S. Tembhurne, F. Nandjou, S. Haussener, *Nat. Energy* **2019**, *4*, 399.

[6] M. Ben-Naim, R. J. Britto, C. W. Aldridge, R. Mow, M. A. Steiner, A. C. Nielander, L. A. King, D. J. Friedman, T. G. Deutsch, J. L. Young, T. F. Jaramillo, *ACS Energy Lett.* **2020**, *5*, 2631.

[7] M. T. Spitler, M. A. Modestino, T. G. Deutsch, C. X. Xiang, J. R. Durrant, D. V. Esposito, S. Haussener, S. Maldonado, I. D. Sharp, B. A. Parkinson, D. S. Ginley, F. A. Houle, T. Hannappel, N. R. Neale, D. G. Nocera, P. C. McIntyre, *Sustainable Energy Fuels* **2020**, *4*, 985.

[8] J. H. Kim, H. E. Kim, J. H. Kim, J. S. Lee, *J. Mater. Chem. A* **2020**, *8*, 9447.

[9] K. Sivula, F. Le Formal, M. Grätzel, *ChemSusChem* **2011**, *4*, 432.

[10] N. Guijarro, P. Bornoz, M. Prévot, X. Yu, X. Zhu, M. Johnson, X. Jeanbourquin, F. Le Formal, K. Sivula, *Sustainable Energy Fuels* **2018**, *2*, 103.

[11] J. H. Kim, Y. J. Jang, S. H. Choi, B. J. Lee, J. H. Kim, Y. Bin Park, C. M. Nam, H. G. Kim, J. S. Lee, *J. Mater. Chem. A* **2018**, *6*, 12693.

[12] V. Celorrio, K. Bradley, O. J. Weber, S. R. Hall, D. J. Fermín, *ChemElectroChem* **2014**, *1*, 1667.

[13] X. Sun, D. Tiwari, D. J. Fermin, *ACS Appl. Mater. Interfaces* **2020**, *12*, 31486.

[14] G. P. Wheeler, K. S. Choi, *ACS Energy Lett.* **2017**, *2*, 2378.

[15] G. P. Wheeler, V. U. Baltazar, T. J. Smart, A. Radmilovic, Y. Ping, K. S. Choi, *Chem. Mater.* **2019**, *31*, 5890.

[16] X. Sun, D. Tiwari, D. J. Fermin, *J. Electrochem. Soc.* **2019**, *166*, H764.

[17] M. I. Díez-García, V. Celorrio, L. Calvillo, D. Tiwari, R. Gómez, D. J. Fermín, *Electrochim. Acta* **2017**, *246*, 365.

[18] J. H. Shah, H. Ye, Y. Liu, A. M. Idris, A. S. Malik, Y. Zhang, H. Han, C. Li, *J. Mater. Chem. A* **2020**, *8*, 6863.

[19] W. Huang, C. Harnagea, X. Tong, D. Benetti, S. Sun, M. Chaker, F. Rosei, R. Nechache, *ACS Appl. Mater. Interfaces* **2019**, *11*, 13185.

[20] S. Y. Yang, J. Seidel, S. J. Byrnes, P. Shafer, C. H. Yang, M. D. Rossell, P. Yu, Y. H. Chu, J. F. Scott, J. W. Ager, L. W. Martin, R. Ramesh, *Nat. Nanotechnol.* **2010**, *5*, 143.

[21] A. Radmilovic, T. J. Smart, Y. Ping, K. S. Choi, *Chem. Mater.* **2020**, *32*, 3262.

[22] D. Tiwari, D. J. Fermin, T. K. Chaudhuri, A. Ray, *J. Phys. Chem. C* **2015**, *119*, 5872.

[23] Y. Ogawa, Y. Kaneko, J. P. He, X. Z. Yu, T. Arima, Y. Tokura, *Phys. Rev. Lett.* **2004**, *92*, 047401.

[24] T. Katayama, S. Yasui, T. Osakabe, Y. Hamasaki, M. Itoh, *Chem. Mater.* **2018**, *30*, 1436.

[25] S. Song, H. M. Jang, N. S. Lee, J. Y. Son, R. Gupta, A. Garg, J. Ratanapreechachai, J. F. Scott, *NPG Asia Mater.* **2016**, *8*, e242.

[26] J. Y. Kim, T. Y. Koo, J. H. Park, *Phys. Rev. Lett.* **2006**, *96*, 047205.

[27] S. K. Mishra, R. Mittal, R. Singh, M. Zbiri, T. Hansen, H. Schober, *J. Appl. Phys.* **2013**, *113*, 174102.

[28] S. Mukherjee, A. Garg, R. Gupta, *J. Phys.: Condens. Matter* **2011**, *23*, 445403.

[29] O. N. Shebanova, P. Lazor, *J. Solid State Chem.* **2003**, *174*, 424.

[30] S. H. Shim, T. S. Duffy, *Am. Mineral.* **2002**, *87*, 318.

[31] S. Ghosh, N. Kamaraju, M. Seto, A. Fujimori, Y. Takeda, S. Ishiwata, S. Kawasaki, M. Azuma, M. Takano, A. K. Sood, *Phys. Rev. B: Condens. Matter Mater. Phys.* **2005**, *71*, 245110.

[32] H. C. Gupta, M. K. Singh, L. M. Tiwari, *J. Raman Spectrosc.* **2002**, *33*, 67.

[33] T. Onuma, S. Fujioka, T. Yamaguchi, Y. Itoh, M. Higashiwaki, K. Sasaki, T. Masui, T. Honda, *J. Cryst. Growth* **2014**, *401*, 330.

[34] A. Thomasson, J. Kreisel, C. Lefèvre, F. Roulland, G. Versini, S. Barre, N. Viart, *J. Phys.: Condens. Matter* **2013**, *25*, 045401.

[35] N. O. Golosova, D. P. Kozlenko, S. E. Kichanov, E. V. Lukin, L. S. Dubrovinsky, A. I. Mammadov, R. Z. Mehdiyeva, S. H. Jabarov, H. P. Liermann, K. V. Glazyrin, T. N. Dang, V. G. Smotrakov, V. V. Eremkin, B. N. Savenko, *J. Alloys Compd.* **2016**, *684*, 352.

[36] H. Yan, Y. Huang, W. Cui, Y. Zhi, D. Guo, Z. Wu, Z. Chen, W. Tang, *Powder Diffr.* **2018**, *33*, 195.

[37] R. K. Ramachandran, J. Dendooven, J. Botterman, S. Pulinthanathu Sree, D. Poelman, J. A. Martens, H. Poelman, C. Detavernier, *J. Mater. Chem. A* **2014**, *2*, 19232.

[38] V. Celorrio, L. Calvillo, C. A. M. van den Bosch, G. Granozzi, A. Aguadero, A. E. Russell, D. J. Fermín, *ChemElectroChem* **2018**, *5*, 3044.

[39] K. A. Stoerzinger, L. Wang, Y. Ye, M. Bowden, E. J. Crumlin, Y. Du, S. A. Chambers, *J. Mater. Chem. A* **2018**, *6*, 22170.

[40] V. Celorrio, L. Calvillo, E. Dann, G. Granozzi, A. Aguadero, D. Kramer, A. E. Russell, D. J. Fermín, *Catal. Sci. Technol.* **2016**, *6*, 7231.

[41] D. M. Sherman, *Phys. Chem. Miner.* **1985**, *12*, 161.

[42] A. Hankin, F. E. Bedoya-Lora, J. C. Alexander, A. Regoutz, G. H. Kelsall, *J. Mater. Chem. A* **2019**, *7*, 26162.

[43] F. H. Taylor, J. Buckeridge, C. R. A. Catlow, *Chem. Mater.* **2016**, *28*, 8210.

[44] C. C. Chueh, C. Z. Li, A. K. Y. Jen, *Energy Environ. Sci.* **2015**, *8*, 1160.

[45] J. Chakrabartty, R. Nechache, C. Harnagea, S. Li, F. Rosei, *Nanotechnology* **2016**, *27*, 215402.

[46] M. I. Díez-García, R. Gómez, *ACS Appl. Mater. Interfaces* **2016**, *8*, 21387.

[47] C. G. Read, Y. Park, K. S. Choi, *J. Phys. Chem. Lett.* **2012**, *3*, 1872.

[48] J. H. Kim, J. H. Kim, J. W. Jang, J. Y. Kim, S. H. Choi, G. Magesh, J. Lee, J. S. Lee, *Adv. Energy Mater.* **2015**, *5*, 1401933.

[49] J. Li, N. Wu, *Catal. Sci. Technol.* **2015**, *5*, 1360.

**ADVANCED
SCIENCE NEWS**

www.advancedsciencenews.com

**ADVANCED
ENERGY
MATERIALS**

www.advenergymat.de

[50] H. Li, Y. Chen, S. Xi, J. Wang, S. Sun, Y. Sun, Y. Du, Z. J. Xu, *Chem. Mater.* **2018**, *30*, 4313.

[51] X. Y. Meng, D. Y. Liu, G. W. Qin, *Energy Environ. Sci.* **2018**, *11*, 692.

[52] D. J. Fermín, E. A. Ponomarev, L. M. Peter, *J. Electroanal. Chem.* **1999**, *473*, 192.

[53] D. K. Lee, D. Lee, M. A. Lumley, K. S. Choi, *Chem. Soc. Rev.* **2019**, *48*, 2126.

[54] W. W. Gärtner, *Phys. Rev.* **1959**, *116*, 84.

[55] J. Li, L. M. Peter, *J. Electroanal. Chem.* **1985**, *193*, 27.

[56] Q. Zhang, V. Celorrio, K. Bradley, F. Eisner, D. Cherns, W. Yan, D. J. Fermín, *J. Phys. Chem. C* **2014**, *118*, 18207.

[57] S. Mukherjee, V. Ranjan, R. Gupta, A. Garg, *Solid State Commun.* **2012**, *152*, 1181.

[58] M. Trassin, N. Viart, G. Versini, S. Barre, G. Pourroy, J. Lee, W. Jo, K. Dumesnil, C. Dufour, S. Robert, *J. Mater. Chem.* **2009**, *19*, 8876.

[59] K. Fountaine, H. Lewerenz, H. Atwater, *Nat. Commun.* **2016**, *7*, 13706.

[60] S. J. Clark, M. D. Segall, C. J. Pickard, P. J. Hasnip, M. I. J. Probert, K. Refson, M. C. Payne, *Z. Kristallogr. - Cryst. Mater.* **2005**, *220*, 567.

[61] M. C. Payne, M. P. Teter, D. C. Allan, T. A. Arias, J. D. Joannopoulos, *Rev. Mod. Phys.* **1992**, *64*, 1045.